ACS APPLIED MATERIALS & INTERFACES

Research Article

www.acsami.org

Hydrogenated TiO_2 Branches Coated Mn_3O_4 Nanorods as an Advanced Anode Material for Lithium Ion Batteries

Nana Wang,[†] Jie Yue,[†] Liang Chen,[†] Yitai Qian,[†,‡] and Jian Yang*,[†]

[†]Key Laboratory of Colloid and Interface Chemistry, Ministry of Education, School of Chemistry and Chemical Engineering Shandong University, Jinan 250100, People's Republic of China

[‡]Hefei National Laboratory for Physical Science at Microscale, Department of Chemistry, University of Science and Technology of China, Hefei 230026, People's Republic of China

Supporting Information

ABSTRACT: Rational design and delicate control on the component, structure, and surface of electrodes in lithium ion batteries are highly important to their performances in practical applications. Compared with various components and structures for electrodes, the choices for their surface are quite limited. The most widespread surface for numerous electrodes, a carbon shell, has its own issues, which stimulates the desire to find another alternative surface. Here, hydrogenated TiO_2 is exemplified as an appealing surface for advanced anodes by the growth of ultrathin hydrogenated TiO_2 branches on Mn_3O_4 nanorods. High theoretical capacity of Mn_3O_4 is well matched with low volume variation (~4%), enhanced electrical conductivity, good cycling stability, and rate capability of hydrogenated TiO_2, as demonstrated in their electrochemical performances. The proof-of-concept reveals the promising potential of hydrogenated TiO_2 as a next-generation material for the surface in high-performance hybrid electrodes.

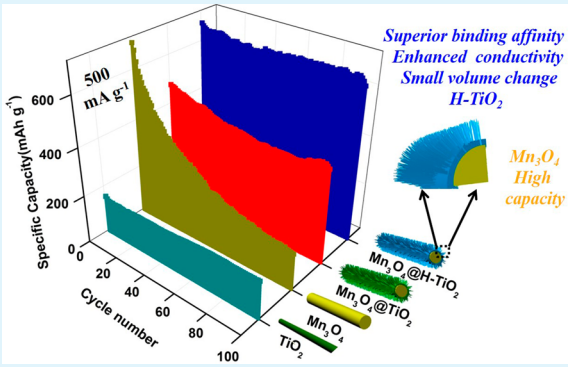

KEYWORDS: *hybrid materials, nanostructures, oxygen vacancies, electrochemical properties, batteries*

INTRODUCTION

Advanced lithium ion batteries (LIBs), as an important link in the chain of sustainable energy applications, have permeated the fields of portable electronics, electric vehicles, and stationary grid storages.[1,2] Although conventional graphite anode has achieved great successes in LIBs, its low capacity (~372 mAh g^{-1} or ~600 mAh cm^{-3}) cannot meet the growing demands of these fields in high energy density and high power density. Thus, the alloy-type anodes, that is, silicon, tin, and their composites, and the conversion-type anodes, basically transitional metal oxides, have been briskly advanced due to their high capacities.[3−5] However, using these materials as anodes also has severe challenges, such as enormous volume change, poor electrical conductivity, large electrode polarization, and unstable solid-electrolyte interphase (SEI). Most of these issues could be mitigated by the fabrication of active materials into various nanostructures coated by a carbon shell. Nanostructures relax the lattice stress/strain and shorten the diffusion distance of lithium. The carbon shell provides a highway for electron transportation and offers a matrix to sustain a stable SEI film upon cycling. Both of them have been demonstrated to be crucial to the electrode performance.

However, there are still a couple of concerns about the carbon shell, such as its layered structures being easily intercalated by solvent molecules, weak binding affinity to active materials, and poor thermal stability.[6−9] Therefore, it is necessary to seek an alternative to carbon as the surface. After an extensive survey on different surface coatings such as In_2O_3, Fe_2O_3, and MnO_2,[10−16] TiO_2 stands out from the others due to its small volume change (only ~4%), excellent cycling stability and rate capability, robust crystal structure to electrolyte, and good thermal stability.[17,18] These features are important for good stability of electrodes in structure and interface.

However, TiO_2 has a poor electrical conductivity (~1×10^{-12} S/m).[19] This fact would greatly retard the transportation of electrons and increase the electrode polarization, leading to capacity degradation.[19] Recently, this issue is mitigated by hydrogenation treatment of TiO_2,[20,21] which could effectively increase the electrical conductivity of TiO_2 by several orders. So, hydrogenated TiO_2, denoted as H-TiO_2, is developed as an advanced anode for LIBs.[22−26] But the reversible capacities of H-TiO_2 alone is still limited. Thus, the growth of H-TiO_2 on high-capacity anodes, like transitional metal oxides as a stable surface, offers a myriad of opportunities to achieve the good cyclability and high capability simultaneously, which has not been reported before to our knowledge. Most importantly, if successful, it opens a door to high-performance electrodes in LIBs.

Received: February 9, 2015
Accepted: April 30, 2015
Published: April 30, 2015

DOI: 10.1021/acsami.5b01208
ACS Appl. Mater. Interfaces 2015, 7, 10348−10355

Here, hydrogenated TiO_2 branches coated Mn_3O_4 nanorods (Mn_3O_4@H-TiO_2) are synthesized as an example to test this concept. In this composite, Mn_3O_4 as a typical transitional metal oxide offers a high theoretical capacity but suffers from severe volume change (~75.4%)[27] and poor electrical conductivity. These issues could be effectively addressed by the growth of H-TiO_2 on its surface because the small volume change and the superior electrical conductivity of H-TiO_2 would improve the SEI stability and the diffusion kinetics simultaneously. Plus, with the good thermal stability and high binding affinity of H-TiO_2 to transitional metal oxides, there is a complete match between Mn_3O_4 and H-TiO_2, which makes them an ideal model to demonstrate the potential of H-TiO_2 as a next-generation material after carbon for high-performance anodes.

RESULTS AND DISCUSSION

Scheme 1 briefly summarizes the synthesis process for Mn_3O_4@H-TiO_2. First, MnOOH nanorods were prepared by a reported hydrothermal reaction,[28] which was confirmed by the XRD pattern in Figure S1a (Supporting Information). Then, SEM and TEM images reveal their narrow size distribution and smooth surface, as indicated in Figure 1a,b. Due to an abundance of hydroxyl groups on the surface, these nanorods show a good dispersity in ethanol, which facilitates the uniform growth of TiO_2 in the next step. The growth of TiO_2 on MnOOH was achieved by a slow hydrolysis of tetrabutyl titanate (TBOT) at a low temperature. As shown in Figure 1c,d, the resultant product keeps the rod-like morphology. Meanwhile, there is a significant increase in diameter from ~80 nm of MnOOH nanorods to ~120 nm of MnOOH@TiO_2 nanorods, indicating the successful coating of TiO_2. The result is also directly validated by the contrast difference in TEM images, which also allows us to estimate the shell thickness of TiO_2 as ~20 nm. Unfortunately, the uniform and continuous shell of TiO_2 is amorphous (Figure S1b, Supporting Information) due to the low reaction temperature.[29]

Scheme 1. Synthesis Process of Mn_3O_4 Nanorods Coated by Hydrogenated TiO_2 Branches (Mn_3O_4@H-TiO_2)

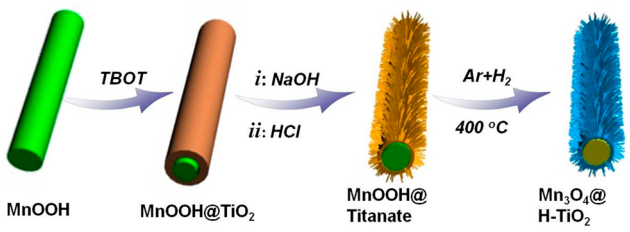

The thick, solid shell of TiO_2 goes against the quick transportation of lithium ions and electrons. Thus, the core–shell nanorods of MnOOH@TiO_2 were treated by NaOH and HCl in turn. Surprisingly, this treatment converted the thick, smooth shell to ultrathin branches on the surface (Figure 1e,f). This huge change could be regarded as the consequence of the following reactions. The first one is the reaction of TiO_2 and NaOH, which produces ultrathin $Na_2Ti_nO_{2n+1}$ branches.[30,31] Then, Na^+ in $Na_2Ti_nO_{2n+1}$ is replaced by H^+ in HCl, generating $H_2Ti_nO_{2n+1}$ for the subsequent annealing to TiO_2.[30,31] Because of the good protection of TiO_2, MnOOH nanorods at the core survive from the treatments, as supported by Figure S1c (Supporting Information). The hierarchical surface structure enables the specific surface area increase from 20.4 $m^2\ g^{-1}$ of MnOOH@TiO_2 to 151.8 $m^2\ g^{-1}$ of MnOOH@titanate (Figure S2, Supporting Information). The calcination of MnOOH@titanate nanorods at 400 °C for 2 h under a reducing atmosphere (Ar/H_2), would result in the formation of Mn_3O_4@H-TiO_2. As stated in Figure S1d (Supporting Information), Mn_3O_4 and H-TiO_2 in Mn_3O_4@H-TiO_2 are in a tetragonal phase (JCPDS card no. 24-0734) and an anatase phase (JCPDS card no. 21-1272), respectively. SEM images indicate that Mn_3O_4@H-TiO_2 well inherit the unique structure from Mn_3O_4@titanate nanorods, as presented by Figure 1g,h. The molar ratio of Mn_3O_4 to H-TiO_2 obtained from EDS spectra (Figure S3, Supporting Information) is approximately about 0.7:1, close to the result from ICP-AES technique. If the calcination temperature is set at 500 °C, Mn_3O_4 would react with TiO_2, leading to impurities like $MnTiO_3$ and hollow structures in the product (Figure S4, Supporting Information).

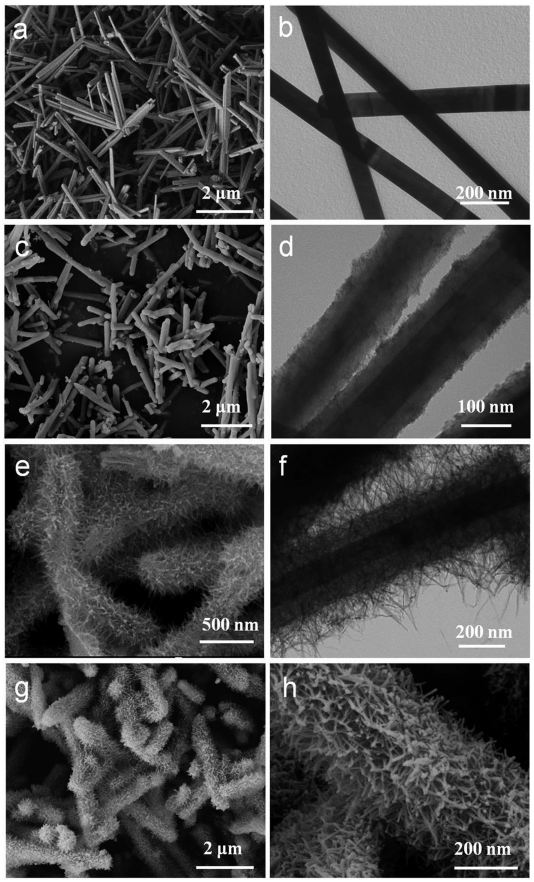

Figure 1. SEM and TEM images of (a and b) MnOOH nanorods, (c and d) MnOOH@TiO_2 nanorods, (e and f) MnOOH@Titanate nanorods, and (g and h) Mn_3O_4@H-TiO_2 nanorods.

Figure 2a shows a typical TEM image of Mn_3O_4@H-TiO_2. The significant contrast in the image could be attributed to the difference between H-TiO_2 and Mn_3O_4 in electron scattering. Compared to H-TiO_2, Mn_3O_4 has a high electron density then an enhanced electron scattering, thus corresponding to the dark nanorod at the center. The light shell related to ultrathin branches is assigned to H-TiO_2. This distribution is also confirmed by elemental mapping and HRTEM images. As shown in Figure 2b, Mn basically locates at the center and Ti

DOI: 10.1021/acsami.5b01208
ACS Appl. Mater. Interfaces 2015, 7, 10348−10355

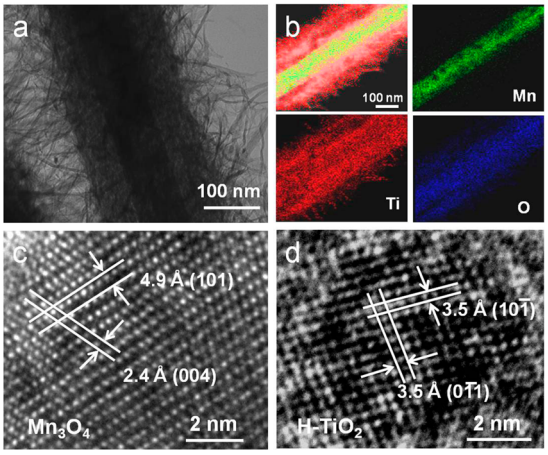

Figure 2. (a) TEM image, (b) elemental mapping, and (c and d) HRTEM images of Mn_3O_4@H-TiO_2.

distributes throughout the surface of the composite. Moreover, the pattern of Ti presents the characteristic of ultrathin branches particularly at the edge of the structure, suggesting the strong correlation between H-TiO_2 and ultrathin branches. HRTEM images on the branches and at the center exhibit clear lattice fringes with their spacings belonging to anatase TiO_2[32] or tetragonal Mn_3O_4 (Figure 2c,d). These results are consistent with the Mn_3O_4 nanorods coated by ultrathin H-TiO_2 branches.

If the annealing step for Mn_3O_4@H-TiO_2 was conducted not in Ar/H_2 but in Ar, the same hybrid structure of Mn_3O_4@TiO_2 could be fabricated and then used as a reference to illustrate the hydrogenation effect. As shown in Figure S5 (Supporting Information), the XRD pattern, SEM and TEM images of Mn_3O_4 @TiO_2 are the same as those of Mn_3O_4@H-TiO_2. The results indicate the negligible influence of hydrogenation treatment on crystal structure and morphology of the product, which is consistent with many reports on TiO_{2-x} or H-TiO_2.[20−24]

However, the hydrogenation treatment alters the chemical status of elements in the product. XPS spectra of Mn_3O_4@H-TiO_2 and Mn_3O_4@TiO_2 are compared to get the insights. Figure 3a shows the survey spectra of Mn_3O_4@H-TiO_2 and Mn_3O_4@TiO_2. Both of them are quite similar, suggesting the signals of Mn, Ti and O in the products. Thus, high-resolution spectra on Mn 2p, Ti 2p, and O 1s are measured to give a close-up check. As shown in Figure 3b, the Mn 2p spectra of Mn_3O_4@H-TiO_2 and Mn_3O_4@TiO_2 are identical, indicating the same bonding environment of Mn in them. This result could be associated with the good surface passivation of TiO_2 to Mn_3O_4 from the influence of different annealing atmospheres. Different from the case of Mn 2p, the spectra of Ti 2p from Mn_3O_4@H-TiO_2 (the top of Figure 3c) exhibit a negative shift in comparison with that of Ti 2p from Mn_3O_4@TiO_2, suggesting a reduced status of Ti in Mn_3O_4@H-TiO_2. This result is supported by the subtraction of the Ti 2p spectrum of Mn_3O_4@H-TiO_2 from that of Mn_3O_4@TiO_2 (the bottom of Figure 3c). The two peaks at 463.4 and 457.7 eV are in good agreement with the characteristic peaks of Ti 2p1/2 and Ti 2p3/2 of Ti^{3+}.[20,21,33−36] To ensure the electrical neutrality of the entire product, there must be oxygen vacancies in H-TiO_2. The two peaks of Ti 2p centered at 464.9 and 458.7 eV is in line with the reported Ti 2p1/2 and Ti 2p3/2 of Ti^{4+}.[20,21,33−36] Figure 3d shows the spectra of O 1s from Mn_3O_4@H-TiO_2 and Mn_3O_4@TiO_2. Both of them exhibit a strong peak at 529.6 eV, which is related to lattice oxygen in Mn_3O_4 and TiO_2.[36,37] The weak shoulder at the high binding energy has been reported to be from Ti−OH.[34] The area ratio of oxygen from the two sources increases from Mn_3O_4@TiO_2 to Mn_3O_4@H-TiO_2, indicating more −OH groups on the surface due to hydrogenation treatment.

The appearance of Ti^{3+} in H-TiO_2 is supposed to induce a pronounced EPR signal, due to its unpaired electron. However, it is difficult to distinguish the signals of Ti^{3+} and Mn^{2+}, because both of them have unpaired electrons and show broad signals overlapping with each other. In spite of this, there are indeed significant differences between the EPR spectra of Mn_3O_4@TiO_2 and Mn_3O_4@H-TiO_2 (Figure S6, Supporting Information). The reliability of our protocol for Ti^{3+} could be demonstrated by a control experiment, in which MnOOH was removed from the protocol and only TiO_2 was formed in the product. As shown in Figure 3e, hydrogenated TiO_2 (H-TiO_2) gives an intense signal, compared to TiO_2 annealed in air. The g factor about 2.004 is close to the typical value of Ti^{3+} in literature,[38−40] indicating the formation of Ti^{3+} induced by the hydrogenation treatment via our protocol. In the Raman spectra (Figure 3f), The Raman characteristic of Mn_3O_4 at 660.2 cm^{-1} is well kept for both Mn_3O_4@H-TiO_2 and Mn_3O_4@TiO_2, suggesting the negligible effect of the hydrogenation treatment on Mn_3O_4.[36] But the Raman signals of TiO_2 after hydrogenation slightly shift to low frequencies, compared to those treated in Ar. The result is in good agreement with the reported oxygen-deficient TiO_2.[20,21]

The appearances of Ti^{3+} along with oxygen vacancies in ultrathin branches induced by hydrogenation treatment, lead to the obvious enhancement of electrochemical properties, although they are tiny changes. Figure 4a shows cyclic voltammograms (CVs) of Mn_3O_4@H-TiO_2 for the first several cycles. There are four peaks for the first cathodic sweep of Mn_3O_4@H-TiO_2 that could be assigned to the insertion of lithium into H-TiO_2 for orthorhombic Li_xTiO_2 (∼1.72 V), the reducing reactions of Mn^{3+} to Mn^{2+} and Mn^{2+} to metallic Mn (∼1.40 and ∼0.15 V), and the formation of solid-electrolyte interphase (SEI) film (∼0.89 V).[41−44] The first anodic sweep gives only three broad peaks at 1.31, 1.70, and 2.06 V. The peak at 1.31 V could be associated with the oxidation of metallic Mn to Mn^{2+} (Figure S7a, Supporting Information). The broad and weak peak at 1.70 V might originate from the partly reversible dissolution of SEI layer.[44] The peak at 2.06 V is probably due to the extraction of Li^+ from Li_xTiO_2. Compared with the case of TiO_2 (Figure S7b, Supporting Information), there is a negative shift for this peak, reflecting the intimate interaction between Mn_3O_4 nanorods and TiO_2 branches. It should be pointed out that such a shift could reduce the electrode polarization and improve the charge-transfer kinetics, enhancing the cycling stability and rate capability of electrode materials. The similar interaction was also observed in our previous work on MnO_2/Fe_2O_3.[12] During the following cathodic sweeps, the reducing reaction of Mn^{2+} to Mn moves to 0.33 V, due to the structure rearrangement. The insertion of lithium into H-TiO_2 is still located at 1.76 V. The anodic sweeps basically overlap with the first, indicating the same electrochemical reaction and good reversibility.

Figure 4b shows the first discharge/charge profiles of Mn_3O_4@H-TiO_2 and Mn_3O_4@TiO_2 in the voltage range of 0.01−3 V at a current density of 500 mA g^{-1}. Both of them exhibit similar discharge/charge behaviors, such as close voltage

DOI: 10.1021/acsami.5b01208
ACS Appl. Mater. Interfaces 2015, 7, 10348−10355

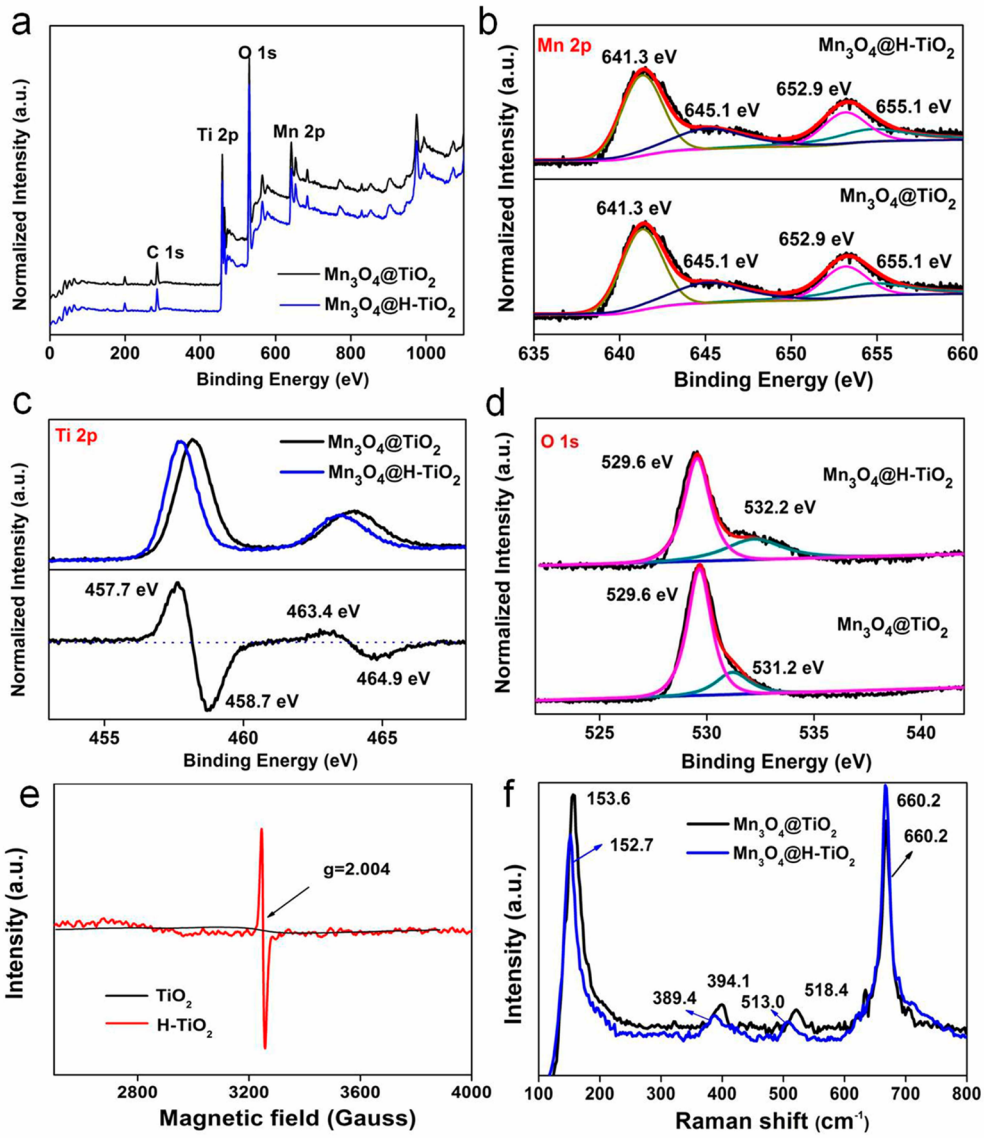

Figure 3. (a) Survey spectra and (b−d) high-resolution spectra on Mn 2p, Ti 2p and O 1s of Mn_3O_4@H-TiO_2 and Mn_3O_4@TiO_2. The difference spectrum of Ti 2p between Mn_3O_4@H-TiO_2 and Mn_3O_4@TiO_2 is shown at the bottom of panel c. (e) EPR spectra of TiO_2 and H-TiO_2 prepared by the same protocols for TiO_2 in Mn_3O_4@TiO_2 and H-TiO_2 in Mn_3O_4@H-TiO_2. (f) Raman spectra of Mn_3O_4@H-TiO_2 and Mn_3O_4@TiO_2 at room temperature.

plateaus, similar specific capacity, and so on. But the Coulombic efficiency of Mn_3O_4@H-TiO_2 for the first cycle (71.2%), is much higher than that of Mn_3O_4@TiO_2 (58.4%), although they have a similar shape, size, and structure. The high Coulombic efficiency of Mn_3O_4@H-TiO_2 originates from an enhanced charge capacity of Mn_3O_4@H-TiO_2, which could be associated with the surface passivation of hydroxyl groups and improved charge-transfer kinetics similar to the carbon shell,[45] due to the hydrogenation treatment for H-TiO_2.

Figure 4c shows the cycling performances of Mn_3O_4@H-TiO_2, Mn_3O_4@TiO_2, TiO_2, and Mn_3O_4 in the range of 0.01−3 V at a current density of 500 mA g^{-1}. Although Mn_3O_4 nanorods (Figure S8, Supporting Information) deliver a specific capacity of 1392 mAh g^{-1} for the first discharge, the capacity quickly falls down to 165 mAh g^{-1} after 100 cycles, suggesting a terrible capacity retention. Compared to the case of Mn_3O_4 nanorods, the specific capacity of TiO_2 nanorods (Figure S8, Supporting Information) only drops for the first several cycles and levels off at 155 mAh g^{-1} until 100 cycles. In view of their low first-discharge capacity (∼330 mAh g^{-1}), TiO_2 show a better capacity retention than Mn_3O_4 nanorods. The combination of the good capacity retention of TiO_2 with the high theoretical capacity of Mn_3O_4 in Mn_3O_4@TiO_2 nanorods realizes the enhancements in both capacity retention and specific capacity. As shown in Figure 4c, the specific capacity of Mn_3O_4@TiO_2 nanorods is promoted to 393 mAh g^{-1} after 100 cycles, much better than those of Mn_3O_4 and TiO_2 nanorods alone. The specific capacity could be further pushed to 615 mAh g^{-1} by Mn_3O_4@ H-TiO_2, which is close to the theoretical capacity based on the mass percentage of components (734.7 mAh g^{-1} = 934 mAh g^{-1} × 66.73 wt % (Mn_3O_4) + 335 mAh g^{-1} × 33.27 wt % (H-TiO_2)). This capacity increase could be assigned to the improved charge-transfer kinetics due to oxygen vacancies in H-TiO_2. The similar conclusion has been well documented for H-TiO_2 or TiO_{2-x} alone as an advanced anode material for LIBs.[22−24] But, to our knowledge, this is the first

DOI: 10.1021/acsami.5b01208
ACS Appl. Mater. Interfaces 2015, 7, 10348−10355

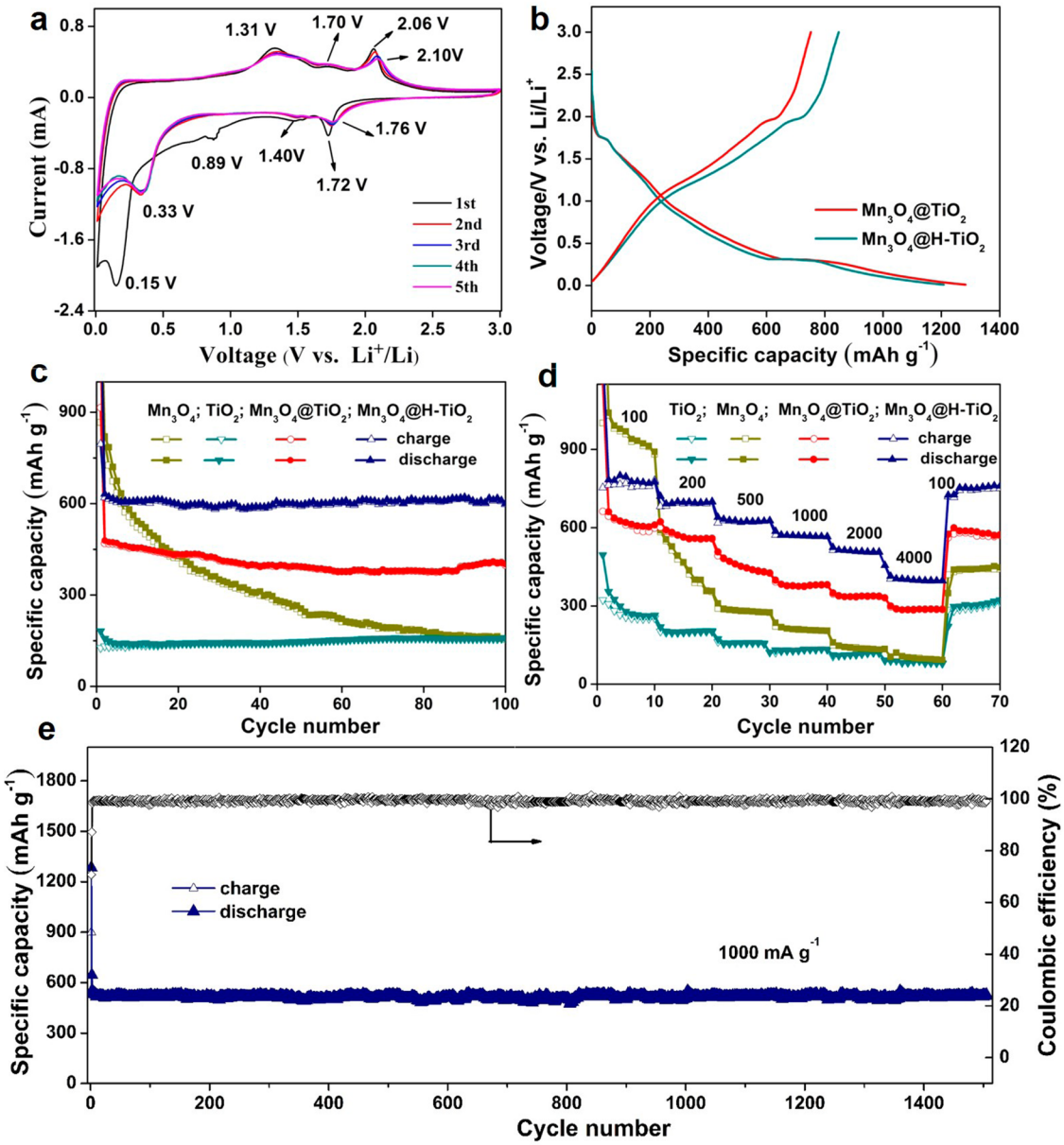

Figure 4. (a) Cyclic voltammograms (CVs) of Mn_3O_4@H-TiO_2 at a scanning rate of 0.1 mV s^{-1}. (b) Discharge−charge curves of Mn_3O_4@H-TiO_2, (c) cycling performances, and (d) rate performances of the electrodes based on Mn_3O_4, TiO_2, Mn_3O_4@TiO_2, and Mn_3O_4@H-TiO_2. (e) Cycling performance of the electrodes based on Mn_3O_4@H-TiO_2 at 1000 mA g^{-1} up to 2000 cycles.

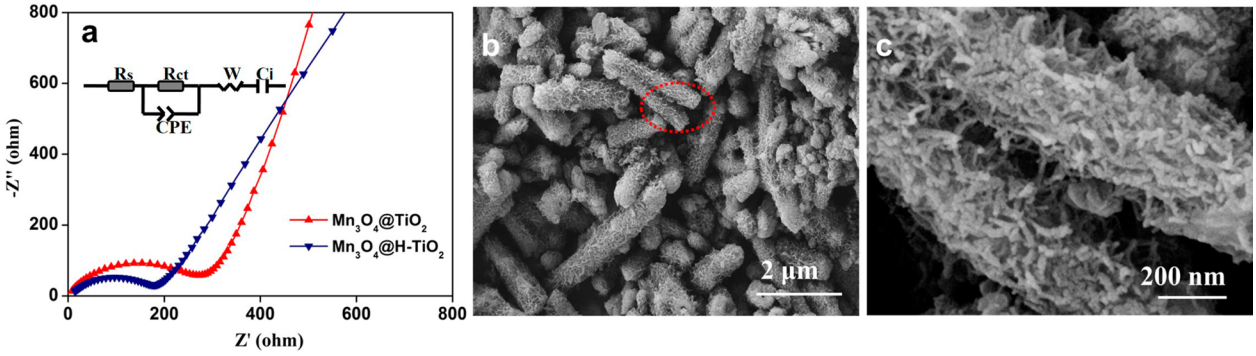

Figure 5. (a) Nyquist plots for the electrodes based on Mn_3O_4@TiO_2 and Mn_3O_4@H-TiO_2 at delithiated state; (inset) equivalent circuit. (b and c) SEM images of Mn_3O_4@H-TiO_2 after 100 cycles at 1 A g^{-1}.

DOI: 10.1021/acsami.5b01208
ACS Appl. Mater. Interfaces 2015, 7, 10348−10355

time it has been used to achieve a good capacity retention and a high specific capacity simultaneously for hybrid nanostructures.

The upgrade of electrochemical properties by H-TiO_2, is also reflected in rate performances, which is supported by the similar comparison between Mn_3O_4@H-TiO_2, Mn_3O_4@TiO_2, Mn_3O_4 and TiO_2. As described in Figure 4d, Mn_3O_4@H-TiO_2 exhibits the reversible capacities of 760, 690, 620, 570, 525, and 431 mAh g^{-1} at the current densities of 100, 200, 500, 1000, 2000, and 4000 mA g^{-1}, much better than those of Mn_3O_4@TiO_2, TiO_2, and Mn_3O_4, particularly at high current densities. As the current density comes back to 100 mA g^{-1}, the specific capacity returns to 750 mAh g^{-1}, indicating a good electrochemical stability. These results are also better than Mn_3O_4 nanoparticles on reduced graphene oxide (RGO) sheets (~390 mAh g^{-1} at 1600 mA g^{-1}),[46] Mn_3O_4 nanoparticles on multiwalled carbon nanotubes (~387 mAh g^{-1} at 1000 mA g^{-1}).[47] Even compared with other transitional metal oxides,[48,49] the rate capability of Mn_3O_4@H-TiO_2 is still impressive. In addition, the specific capacity of Mn_3O_4@H-TiO_2 nanorods stays at 560 mAh g^{-1} even after 2000 cycles at 1 A g^{-1}, as shown in Figure 4e. This excellent cycling stability is highly desirable for the potential application of anode materials. To the best of our knowledge, this is the longest cycle life for Mn_3O_4 or the related hybrids. Most of the works on Mn_3O_4 anodes only reported its short-term cyclability (≤150 cycles) at a low current density (≤200 mA g^{-1}; Table S1, Supporting Information).[43,46,47,50−58] Moreover, the capacity in our case could be further elevated by reducing the ratio of H-TiO_2 in the nanocomposite.

The enhanced performance via H-TiO_2 in Mn_3O_4@H-TiO_2 is supported by electrochemical impedance spectra (EIS). As shown in Figure 5a, the spectra consist of one depressed semicircle in the high frequency region connected to a slope in the low frequency region. The depressed semicircle reflects the ohmic resistance (R_s) and the charge-transfer resistance (R_{ct}) at the interface. The slope is related to the lithium diffusion inside electrode, which is usually evaluated by Warburg resistance (Z_w). CPE in the equivalent circuit is constant phase element, and C_i is the intercalation capacitance. Compared to Mn_3O_4@TiO_2, Mn_3O_4@H-TiO_2 exhibits the smaller R_{ct}, reflecting its better charge-transfer kinetics. The superior charge-transfer kinetics of Mn_3O_4@H-TiO_2 is also supported by the comparison with TiO_2 and Mn_3O_4 (Figure S9, Supporting Information). The same conclusion could be realized by direct-current resistance (Figure S9 Supporting Information). Mn_3O_4@H-TiO_2 manifests a lower direct-current resistance than TiO_2, Mn_3O_4, and Mn_3O_4@TiO_2, no matter its state of charge/discharge. As shown in Figure 5b,c, Mn_3O_4@H-TiO_2 basically preserves its rod-like shape and unique branches on the surface after 100 cycles at 1 A g^{-1}, indicating the good stability of Mn_3O_4@H-TiO_2 during the repeated lithiation/delithiation.

The excellent cycling stability and rate capability of Mn_3O_4@H-TiO_2 are associated with their unique structure, rational surface design, and successful formation of oxygen vacancies. First, from a structure viewpoint, ultrathin branches on the nanorods greatly increase the contact between electrode and electrolyte, reduce the overpotentials of lithium insertion/extraction, and improve the reaction kinetics. Meanwhile, the nanoscale size of these building blocks effectively shortens the lithium diffusion pathway and benefits the release of the strain/stress caused by lithium insertion/extraction. Second, from an interface viewpoint, TiO_2 as an anode exhibit an excellent cycling stability and a small volume change (~4%), both of which are highly desirable for those high-capacity anodes with a huge volume change and bad cycling stability. Using TiO_2 as an interface between these anodes and electrolyte could realize the stable interface between electrode and electrolyte and sustain the electrode structure upon cycling. Third, the formation of oxygen vacancies in H-TiO_2 remarkably promotes the electrical conductivity and lowers charge-transfer resistance and direct-current resistances of the entire hybrid, all of which enhance the diffusion kinetics and improve the electrochemical properties. The synergistic effect of these results enables Mn_3O_4@H-TiO_2 to be a promising anode for advanced LIBs. Most importantly, this concept offers a novel and reliable route to improve the electrochemical properties of many known anodes.

■ CONCLUSION

Mn_3O_4 nanorods coated by hydrogenated TiO_2 branches are successfully synthesized by a multistep process, involving a hydrothermal reaction for MnOOH nanorods, low-temperature hydrolysis for the growth of a TiO_2 shell on MnOOH, alkaline and acid treatments to generate ultrathin branches on MnOOH, and moderate annealing in Ar/H_2 for Mn_3O_4@H-TiO_2. This unique hybrid nanostructure combines high theoretical capacity of Mn_3O_4 with stable electrochemical properties, small volume change, and relatively good electrical conductivity of H-TiO_2, realizing the complementary components of the hybrid. As expected, Mn_3O_4@H-TiO_2 exhibits significant enhancements in cycling stability and rate capability, compared with Mn_3O_4, TiO_2, and Mn_3O_4@TiO_2. After 2000 cycles at a rate of 1 A g^{-1}, they could still maintain 560 mAh g^{-1}. The superior performance could be attributed to proper selection of chemical components in hybrid and effective controls on size and structure of hybrid. These results pave the way for the extensive application of hydrogenated TiO_2 as an alternative to carbon in high-performance anodes in lithium ion batteries.

■ EXPERIMENTAL SECTION

Synthesis of MnOOH. MnOOH nanorods were synthesized on the basis of our previous report.[25] Briefly, 0.1 g of $KMnO_4$ and 2 mL of polyethylene glycol were added into 40 mL of deionized water. After stirring for 30 min, the solution was heated to 160 °C for 5 h in a sealed Teflon-lined autoclave with a capacity of 50 mL. The final product was collected by filtration and washed with deionized water and ethanol three times.

Syntheses of Mn_3O_4@TiO_2 and Mn_3O_4@H-TiO_2. A typical synthesis was illustrated by Scheme 1. First, 0.15 g of the as-obtained MnOOH nanorods was dispersed in 200 mL of ethanol first. Then, 0.9 mL of 28 wt % ammonia was dropped into the solution. The solution was sonicated for 30 min to ensure the good dispersity of MnOOH during the next reaction. After that, 2 mL of TBOT was added as a precursor for the growth of TiO_2 on MnOOH. The solution was heated to 45 °C for 24 h to accelerate the hydrolysis of TBOT. The resultant product, MnOOH@TiO_2 nanorods, was collected and washed with deionized water. Afterward, the synthesized MnOOH@TiO_2 nanorods (0.05g) were treated by 20 mL of 2 M NaOH at 45 °C for 16 h and then 50 mL of 0.1 M HCl at room temperature for 20 min. The TiO_2 shell was converted into titanate. Due to the good protection by titanate, MnOOH nanorods were well kept after these reactions. Annealing the MnOOH@Titanate nanorods in Ar or Ar/H_2 (5% H_2 and 95% Ar) at 400 °C for 2 h produced the nanorods of Mn_3O_4@TiO_2 or Mn_3O_4@ H-TiO_2.

Sample Characterization. X-ray diffraction (XRD) patterns were recorded on a Bruker D8 advanced X-ray diffractometer, using Cu Kα radiation with λ = 1.5418 Å. Transmission electron microscopy

DOI: 10.1021/acsami.5b01208
ACS Appl. Mater. Interfaces 2015, 7, 10348−10355

(TEM) images and field-emission scanning electron microscopy (FESEM) images were achieved from a transmission electron microscope (JEOL JEM 1011) and a field-emission scanning electron microscope (SUPRA 55). HRTEM images were acquired on an analytic transmission electron microscopy (JEOL-2100F). An inductive coupled plasma atomic emission spectrometer (IRIS Inrtrepid II XSP) was used to analyze the chemical composition. Nitrogen sorption isotherms were examined on a Micromeritics ASAP-2020HD88 instrument. Raman spectra were obtained from a NEXUS 670 Micro-Raman Spectrometer. X-ray photoelectron spectrometry (XPS) spectra were measured on X-ray photoelectron spectrometer (ESCALAB 250) by referencing the C 1s peak to 284.6 eV. The electron paramagnetic resonance (EPR) spectra were acquired on a JEOL JES FA200 EPR spectrometer (77 K).

Electrochemical Measurements. The working electrode was made by 70 wt % active material, 20 wt % conductive carbon black and 10 wt % sodium salt of caboxymethyl cellulose (CMC). The powders were dispersed in several droplets of deionized water and milled for 30 min, producing a black slurry. The slurry was then spread on a copper foil using a stainless steel blade with a wet film thickness of 200 μm and dried overnight under vacuum at 60 °C. The typical loading of the active material was in the range of 1−2 mg cm^{-1}. The foil was roll-pressed and punched into discs with a diameter of 12 mm. After that, the discs were assembled in an argon-filled glovebox (Mikrouna, Super 1220/750/900) with Li foil as the counter/reference electrode, a Celgard 2400 membrane as the separator, and 1 M $LiPF_6$ in a mixture of ethylene carbonate (EC), diethyl carbonate (DEC) and dimethyl carbonate (DMC; 1:1:1, v/v/v) as the electrolyte. Galvanostatic charge−discharge cycles were conducted on Land-CT2001A battery cyclers (Wuhan, China). Cyclic voltammograms (CV) profiles were obtained on a LK2005A electrochemical workstation (Tianjin China) in a range of 0.01−3 V at a scanning rate of 0.1 mV s^{-1}. Direct current (dc) resistance was measured at every 5% variation of depth of discharge (DOD) or state of charge (DOC) of the electrode. Electrochemical impedance spectra (EIS) were acquired from an AUTOLAB PGSTAT204 electrochemical workstation over the frequency range of 100 kHz to 0.01 Hz.

■ ASSOCIATED CONTENT

Supporting Information

Additional experimental data as described in text. The Supporting Information is available free of charge on the ACS Publications website at DOI: 10.1021/acsami.5b01208.

■ AUTHOR INFORMATION

Corresponding Author

*E-mail: yangjian@sdu.edu.cn. Tel.: +86 531 88364489.

Notes

The authors declare no competing financial interest.

■ ACKNOWLEDGMENTS

This work was supported by the 973 Project of China (No. 2011CB935901), the National Nature Science Foundation of China (No. 91022033, 51172076, and 21471090), Shandong Provincial Natural Science Foundation for Distinguished Young Scholar (JQ201205), Independent Innovation Foundations of Shandong University (2012ZD007), and new faculty start-up funding in Shandong University. We also thank Prof. Yang Liu from State Key Lab of Crystal Materials.

■ REFERENCES

(1) Armand, M.; Tarascon, J. M. Building Better Batteries. *Nature* **2008**, *451*, 652−657.

(2) Bruce, P. G.; Scrosati, B.; Tarascon, J. M. Nanomaterials for Rechargeable Lithium Batteries. *Angew. Chem., Int. Ed.* **2008**, *47*, 2930−2946.

(3) Liu, N.; Wu, H.; McDowell, M. T.; Yao, Y.; Wang, C. M.; Cui, Y. A Yolk-Shell Design for Stabilized and Scalable Li-Ion Battery Alloy Anodes. *Nano Lett.* **2012**, *12*, 3315−3321.

(4) Zhu, Z. Q.; Wang, S. W.; Du, J.; Jin, Q.; Zhang, T. R.; Cheng, F. Y.; Chen, J. Ultrasmall Sn Nanoparticles Embedded in Nitrogen-Doped Porous Carbon as High-Performance Anode for Lithium-Ion Batteries. *Nano Lett.* **2014**, *14*, 153−157.

(5) Wu, H. B.; Chen, J. S.; Hng, H. H.; Lou, X. W. Nanostructured Metal Oxide-based Materials as Advanced Anodes for Lithium-Ion Batteries. *Nanoscale* **2012**, *4*, 2526−2542.

(6) Evanoff, K.; Magasinski, A.; Yang, J. B.; Yushin, G. Nanosilicon-Coated Graphene Granules as Anodes for Li-Ion Batteries. *Adv. Energy Mater.* **2011**, *1*, 495−498.

(7) Abouimrane, A.; Compton, O. C.; Amine, K.; Nguyen, S. T. Non-Annealed Graphene Paper as a Binder-Free Anode for Lithium-Ion Batteries. *J. Phys. Chem. C* **2010**, *114*, 12800−12804.

(8) Pan, D. Y.; Wang, S.; Zhao, B.; Wu, M. H.; Zhang, H. J.; Wang, Y.; Jiao, Z. Li Storage Properties of Disordered Graphene Nanosheets. *Chem. Mater.* **2009**, *21*, 3136−3142.

(9) Evanoff, K.; Benson, J.; Schauer, M.; Kovalenko, I.; Lashmore, D.; Jud Ready, W.; Yushin, G. Ultra Strong Silicon-Coated Carbon Nanotube Nonwoven Fabric as a Multifunctional Lithium-Ion Battery Anode. *ACS Nano* **2012**, *11*, 9837−9845.

(10) Kim, D. W.; Hwang, I. S.; Kwon, S. J.; Kang, H. Y.; Park, K. S.; Choi, Y. J.; Choi, K. J.; Park, J. G. Highly Conductive Coaxial SnO_2-In_2O_3 Heterostructured Nanowires for Li Ion Battery Electrodes. *Nano Lett.* **2007**, *7*, 3041−3045.

(11) Zhou, W. W.; Cheng, C. W.; Liu, J. P.; Tay, Y. Y.; Jiang, J.; Jia, X. T.; Zhang, J. X.; Gong, H.; Hng, H. H.; Yu, T.; Fan, H. J. Epitaxial Growth of Branched α-Fe_2O_3/SnO_2 Nano-Heterostructures with Improved Lithium-Ion Battery Performance. *Adv. Funct. Mater.* **2011**, *21*, 2439−2445.

(12) Gu, X.; Chen, L.; Ju, Z. C.; Xu, H. Y.; Yang, J.; Qian, Y. T. Controlled Growth of Porous α-Fe_2O_3 Branches on β-MnO_2 Nanorods for Excellent Performance in Lithium-Ion Batteries. *Adv. Funct. Mater.* **2013**, *23*, 4049−4056.

(13) Kong, D. Z.; Luo, J. S.; Wang, Y. L.; Ren, W. N.; Yu, T.; Luo, Y. S.; Yang, Y. P.; Cheng, C. W. Three-Dimensional Co_3O_4@MnO_2 Hierarchical Nanoneedle Arrays: Morphology Control and Electrochemical Energy Storage. *Adv. Funct. Mater.* **2014**, *24*, 3815−3826.

(14) Wu, X. M.; Zhang, S. C.; Wang, L. L.; Du, Z. J.; Fang, H.; Ling, Y. H.; Huang, Z. H. Coaxial SnO_2@TiO_2 Nanotube Hybrids: from Robust Assembly Strategies to Potential Application in Li^+ Storage. *J. Mater. Chem.* **2012**, *22*, 11151−11158.

(15) Jeun, J. H.; Park, K. Y.; Kim, D. H.; Kim, W. S.; Kim, H. C.; Lee, B. S.; Kim, H.; Yu, W. R.; Kang, K.; Hong, S. H. SnO_2@TiO_2 Double-Shell Nanotubes for a Lithium Ion Battery Anode with Excellent High Rate Cyclability. *Nanoscale* **2013**, *5*, 8480−8483.

(16) Zhang, X.; Chen, H. X.; Xie, Y. P.; Guo, J. X. Ultralong Life Lithium-Ion Batteries Anode with Superior High-Rate Capability and Excellent Cyclic Stability from Mesoporous Fe_2O_3@TiO_2 Core-Shell Nanorods. *J. Mater. Chem. A* **2014**, *2*, 3912−3918.

(17) Deng, D.; Kim, M. G.; Lee, J. Y.; Cho, J. Green Energy Storage Materials: Nanostructured TiO_2 and Sn-based Anodes for Lithium-Ion Batteries. *Energy Environ. Sci.* **2009**, *2*, 818−837.

(18) Perego, C.; Revel, R.; Durupthy, O.; Cassaignon, S.; Jolivet, J. P. Thermal Stability of TiO_2-Anatase: Impact of Nanoparticles Morphology on Kinetic Phase Transformation. *Solid State Sci.* **2010**, *12*, 989−995.

(19) Song, T.; Han, H.; Choi, H.; Lee, J. W.; Park, H.; Lee, S.; Park, W.; Kim, S.; Liu, L.; Paik, U. TiO_2 Nanotubes Branched Tree on Carbon Nanofiber Nanostructure as an Anode for High Energy and Power Lithium Ion Batteries. *Nano Res.* **2014**, *7*, 491−501.

(20) Lu, X. H.; Wang, G. M.; Zhai, T.; Yu, M. H.; Gan, J. Y.; Tong, Y. X.; Li, Y. Hydrogenated TiO_2 Nanotube Arrays for Supercapacitors. *Nano Lett.* **2012**, *12*, 1690−1696.

(21) Lu, X. H.; Yu, M. H.; Wang, G. M.; Zhai, T.; Xie, S. L.; Ling, Y. C.; Tong, Y. X.; Li, Y. H-TiO_2@MnO_2//H-TiO_2@C Core-Shell

DOI: 10.1021/acsami.5b01208
ACS Appl. Mater. Interfaces 2015, 7, 10348−10355

Nanowires for High Performance and Flexible Asymmetric Supercapacitors. *Adv. Mater.* **2013**, *25*, 267−272.
(22) Shin, J. Y.; Joo, J. H.; Samuelis, D.; Maier, J. Oxygen-Deficient $TiO_{2-\delta}$ Nanoparticles via Hydrogen Reduction for High Rate Capability Lithium Batteries. *Chem. Mater.* **2012**, *24*, 543−551.
(23) Lu, Z. G.; Yip, C. T.; Wang, L. P.; Huang, H. T.; Zhou, L. M. Hydrogenated TiO_2 Nanotube Arrays as High-Rate Anodes for Lithium-Ion Microbatteries. *ChemPlusChem.* **2012**, *77*, 991−1000.
(24) Xia, T.; Zhang, W.; Murowchick, J. B.; Liu, G.; Chen, X. B. A Facile Method to Improve the Photocatalytic and Lithium-ion Rechargeable Battery Performance of TiO_2 Nanocrystals. *Adv. Energy Mater.* **2013**, *3*, 1516−1523.
(25) Li, S.; Qiu, J. X.; Ling, M.; Peng, F.; Wood, B.; Zhang, S. Q. Photoelectrochemical Characterization of Hydrogenated TiO_2 Nanotubes as Photoanodes for Sensing Applications. *ACS Appl. Mater. Interfaces* **2013**, *5*, 11129−11135.
(26) Qiu, J. X.; Li, S.; Gray, E.; Liu, H. W.; Gu, Q. F.; Sun, C. H.; Lai, C.; Zhao, H. J.; Zhang, S. Q. Hydrogenation Synthesis of Blue TiO_2 for High-Performance Lithium-Ion Batteries. *J. Phys. Chem. C* **2014**, *118*, 8824−8830.
(27) Ponrouch, A.; Taberna, P. L.; Simon, P.; Palacín, M. R. On the Origin of the Extra Capacity at Low Potential in Materials for Li Batteries Reacting Through Conversion Reaction. *Electrochim. Acta* **2012**, *61*, 13−18.
(28) Bai, Z. C.; Sun, B.; Fan, N.; Ju, Z. C.; Li, M. H.; Xu, L. Q.; Qian, Y. T. Branched Mesoporous Mn_3O_4 Nanorods: Facile Synthesis and Catalysis in the Degradation of Methylene Blue. *Chem.—Eur. J.* **2012**, *18*, 5319−5324.
(29) Li, W.; Deng, Y. H.; Wu, Z. X.; Qian, X. F.; Yang, J. P.; Wang, Y.; Gu, D.; Zhang, F.; Tu, B.; Zhao, D. Y. Hydrothermal Etching Assisted Crystallization: a Facile Route to Functional Yolk-Shell Titanate Microspheres with Ultrathin Nanosheets-Assembled Double Shells. *J. Am. Chem. Soc.* **2011**, *133*, 15830−15833.
(30) Kasuga, T.; Hiramastu, M.; Hoson, A.; Sekino, T.; Niihara, K. Formation of Titanium Oxide Nanotube. *Langmuir* **1998**, *14*, 3160−3163.
(31) Wang, X. D.; Li, Z. D.; Shi, J.; Yu, Y. H. One-Dimensional Titanium Dioxide Nanomaterials: Nanowires, Nanorods, and Nanobelts. *Chem. Rev.* **2014**, *114*, 9346−9384.
(32) Ding, K. L.; Miao, Z. J.; Liu, Z. M.; Zhang, Z. F.; Han, B. X.; An, G. M.; Miao, S. D.; Xie, Y. Facile Synthesis of High Quality TiO_2 Nanocrystals in Ionic Liquid via a Microwave-Assisted Process. *J. Am. Chem. Soc.* **2007**, *129*, 6362−6363.
(33) Chen, X. B.; Liu, L.; Yu, P. Y.; Mao, S. S. Increasing Solar Absorption for Photocatalysis with Black Hydrogenated Titanium Dioxide Nanocrystals. *Science* **2011**, *331*, 746−750.
(34) Lazarus, M. S.; Sham, T. K. X-ray Photoelectron Spectroscopy (XPS) Studies of Hydrogen Reduced Rutile (TiO_{2-x}) Surfaces. *Chem. Phys. Lett.* **1982**, *92*, 670−674.
(35) Werfel, F.; Brummer, O. Corundum Structure Oxides Studied by XPS. *Phys. Scr.* **1983**, *28*, 92−96.
(36) McCafferty, E.; Wightman, J. P. Determination of the Concentration of Surface Hydroxyl Groups on Metal Oxide Films by a Quantitative XPS Method. *Surf. Interface Anal.* **1998**, *26*, 549−564.
(37) Tan, B. J.; Klabunde, K. J.; Sherwood, P. M. A. XPS Studies of Solvated Metal Atom Dispersed Catalysts Evidence for Layered Cobalt-Manganese Particles on Alumina and Silica. *J. Am. Chem. Soc.* **1991**, *113*, 855−861.
(38) Nakamura, I.; Negishi, N.; Kutsna, S.; Ihara, T.; Sugihara, S.; Takeuchi, K. Role of Oxygen Vacancy in the Plasma-Treated TiO_2 Photocatalyst with Visible Light Activity for NO Removal. *J. Mol. Catal. A: Chem.* **2000**, *161*, 205−212.
(39) Xia, T.; Zhang, W.; Murowchick, J.; Liu, G.; Chen, X. B. Built-in Electric Field-Assisted Surface-Amorphized Nanocrystals for High-Rate Lithium-Ion Battery. *Nano Lett.* **2013**, *13*, 5289−5296.
(40) Liu, N.; Schneider, C.; Freitag, D.; Hartmann, M.; Venkatesan, U.; Müller, J.; Spiecker, E.; Schmuki, P. Black TiO_2 Nanotubes: Cocatalyst-Free Open-Circuit Hydrogen Generation. *Nano Lett.* **2014**, *14*, 3309−3313.
(41) Xu, H. Y.; Xu, S. L.; Wang, H.; Yan, H. Characterization of Hausmannite Mn_3O_4 Thin Films by Chemical Bath Deposition. *J. Electrochem. Soc.* **2005**, *152*, C803−C807.
(42) Luo, J. S.; Xia, X. H.; Luo, Y. S.; Guan, C.; Liu, J. L.; Qi, X. Y.; Ng, C. F.; Yu, T.; Zhang, H.; Fan, H. J. Rationally Designed Hierarchical TiO_2@Fe_2O_3 Hollow Nanostructures for Improved Lithium Ion Storage. *Adv. Energy Mater.* **2013**, *3*, 737−743.
(43) Bai, Z. C.; Fan, N.; Ju, Z. C.; Guo, C. L.; Qian, Y. T.; Tang, B.; Xiong, S. L. Facile Synthesis of Mesoporous Mn_3O_4 Nanotubes and their Excellent Performance for Lithium-Ion Batteries. *J. Mater. Chem. A* **2013**, *1*, 10985−10990.
(44) Grugeon, S.; Laruelle, S.; Herrera-Urbina, R.; Dupont, L.; Poizot, P.; Tarascon, J. M. Particle Size Effects on the Electrochemical Performance of Copper Oxides toward Lithium. *J. Electrochem. Soc.* **2001**, *148*, A285−A292.
(45) Fu, L. J.; Liu, H.; Zhang, H. P.; Li, C.; Zhang, T.; Wu, Y. P.; Holze, R.; Wu, H. Q. Synthesis and Electrochemical Performance of Novel Core/Shell Structured Nanocomposites. *Electrochem. Commun.* **2006**, *8*, 1−4.
(46) Wang, H. L.; Cui, L. F.; Yang, Y.; Casalongue, H. S.; Robinson, J. T.; Liang, Y. Y.; Cui, Y.; Dai, H. J. Mn_3O_4-Graphene Hybrid as a High-Capacity Anode Material for Lithium Ion Batteries. *J. Am. Chem. Soc.* **2010**, *132*, 13978−13980.
(47) Wang, Z. H.; Yuan, L. X.; Shao, Q. G.; Huang, F.; Huang, Y. H. Mn_3O_4 Nanocrystals Anchored on Multi-Walled Carbon Nanotubes as High-Performance Anode Materials for Lithium-Ion Batteries. *Mater. Lett.* **2012**, *80*, 110−113.
(48) Wang, B.; Cheng, J. L.; Wu, Y. P.; Wang, D.; He, D. N. Porous NiO Fibers Prepared by Electrospinning as High Performance Anode Materials for Lithium Ion Batteries. *Electrochem. Commun.* **2012**, *23*, 5−8.
(49) Poizot, P.; Laruelle, S.; Grugeon, S.; Dupont, L.; Tarascon, J. M. Nano-Sized Transition-Metal Oxides as Negative-Electrode Materials for Lithium-Ion Batteries. *Nature* **2000**, *407*, 496−499.
(50) Gao, J.; Lowe, M. A.; Abruña, H. D. Spongelike Nanosized Mn_3O_4 as a High-Capacity Anode Material for Rechargeable Lithium Batteries. *Chem. Mater.* **2011**, *23*, 3223−3227.
(51) Huang, S. Z.; Jin, J.; Cai, Y.; Li, Y.; Tan, H. Y.; Wang, H. E.; Tendeloo, G. V.; Su, B. L. Engineering Single Crystalline Mn_3O_4 Nano-Octahedra with Exposed Highly Active {101} Facets for High Performance Lithium Ion Batteries. *Nanoscale* **2014**, *6*, 6819−6827.
(52) Jian, G. Q.; Xu, Y. H.; Lai, L. C.; Wang, C. S.; Zachariah, M. R. Mn_3O_4 Hollow Spheres for Lithium-Ion Batteries with High Rate and Capacity. *J. Mater. Chem. A* **2014**, *2*, 4627−4632.
(53) Wang, C. B.; Yin, L. W.; Xiang, D.; Qi, Y. X. Uniform Carbon Layer Coated Mn_3O_4 Nanorod Anodes with Improved Reversible Capacity and Cyclic Stability for Lithium Ion Batteries. *ACS Appl. Mater. Interfaces* **2012**, *4*, 1636−1642.
(54) Li, L.; Guo, Z. P.; Du, A. J.; Liu, H. K. Rapid Microwave-Assisted Synthesis of Mn_3O_4-Graphene Nanocomposite and its Lithium Storage Properties. *J. Mater. Chem.* **2012**, *22*, 3600−3605.
(55) Nam, I.; Kim, N. D.; Kim, G. P.; Park, J. S.; Yi, J. H. One Step Preparation of Mn_3O_4/Graphene Composites for Use as an Anode in Li Ion Batteries. *J. Power Sources* **2013**, *244*, 56−52.
(56) Li, Z. Q.; Liu, N. N.; Wang, X. K.; Wang, C. B.; Qi, Y. X.; Yin, L. W. Three-Dimensional Nanohybrids of Mn_3O_4/Ordered Mesoporous Carbons for High Performance Anode Materials for Lithium-Ion Batteries. *J. Mater. Chem.* **2012**, *22*, 16640−16648.
(57) Liu, S. Y.; Xie, J.; Zheng, Y. X.; Cao, G. S.; Zhu, T. J.; Zhao, X. B. Nanocrystal Manganese Oxide (Mn_3O_4, MnO) Anchored on Graphite Nanosheet with Improved Electrochemical Li-Storage Properties. *Electrochim. Acta* **2012**, *66*, 271−278.
(58) Wang, J. Z.; Du, N.; Wu, H.; Zhang, H.; Yu, J. X.; Yang, D. R. Order-Aligned Mn_3O_4 Nanostructures as Super High-Rate Electrodes for Rechargeable Lithium-Ion Batteries. *J. Power Sources* **2013**, *222*, 32−37.

DOI: 10.1021/acsami.5b01208
ACS Appl. Mater. Interfaces 2015, 7, 10348−10355